ACS APPLIED MATERIALS & INTERFACES

Research Article

Cite This: ACS Appl. Mater. Interfaces 2019, 11, 3196−3206

www.acsami.org

Efficient MOF-Sensitized Solar Cells Featuring Solvothermally Grown [100]-Oriented Pillared Porphyrin Framework-11 Films on ZnO/FTO Surfaces

Monica A. Gordillo,[†] Dillip K. Panda,[†] and Sourav Saha*

Department of Chemistry, Clemson University, Clemson, South Carolina 29634, United States

Supporting Information

ABSTRACT: Owing to their abilities to assemble and organize a large number of redox and photoactive components in highly ordered periodic fashion, crystalline porous metal−organic frameworks (MOFs) have the potential to execute myriad complex functions, including charge transport and light to electrical energy conversion when the required conditions are fulfilled. Herein, we demonstrate an unprecedented spontaneous solvothermal growth of precisely [100]-oriented pillared porphyrin framework-11 (PPF-11) films featuring vertically aligned Zn-tetrakis(4-carboxyphenyl)porphyrin (ZnTCPP) walls and horizontally aligned 2,2′-dimethyl-4,4′-bipyridine beams attached to annealed ZnO−fluorine-doped tin oxide (FTO) surfaces and their remarkable photovoltaic performance in liquid-junction solar cells. The [100]-oriented PPF-11/ZnO−FTO photoanodes displayed excellent photovoltaic response (short-circuit current (J_{SC}): 4.65 mA/cm^2, open-circuit voltage (V_{OC}): 470 mV, power conversion efficiency: 0.86%) that easily outperformed all control devices as well as previously reported porphyrin and Ru(bpy)$_3^{2+}$-based visible light-harvesting MOFs with 10−1000 times greater photocurrent density and 2−375 times higher efficiency. The superior photovoltaic behavior of [100]-oriented PPF-11/ZnO films compared to epitaxially grown MOF thin films on insulating self-assembled monolayers and drop-cast PPF films with different orientations can be attributed to several factors, including better charge separation, transport, and injection capabilities of the former. The noncatenated PPF-11 was able to host electron-deficient C_{60} guests, filling in nearly half of its cavities and engage them in ZnTCPP/C_{60} charge-transfer interaction. However, the C_{60}-doped PPF-11/ZnO films displayed much weaker photovoltaic response than undoped [100]-oriented PPF-11/ZnO films presumably due to exclusion of I^-/I_3^- electrolyte from the C_{60}-occupied cavities and the inability of isolated C_{60} guests to support long-range charge movement.

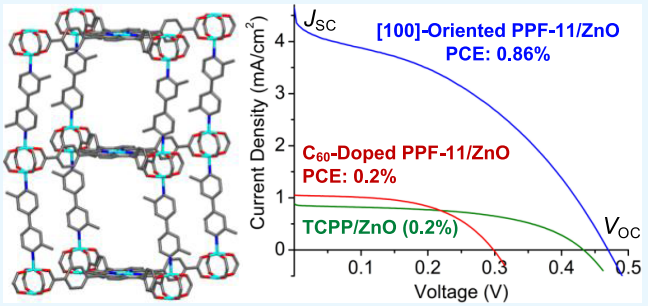

KEYWORDS: *pillared porphyrin frameworks, oriented MOF film, light-harvesting, photovoltaic response, solar cells*

Downloaded via CLEMSON UNIV on April 24, 2019 at 20:23:29 (UTC).
See https://pubs.acs.org/sharingguidelines for options on how to legitimately share published articles.

INTRODUCTION

The skyrocketing energy demand and intensifying global initiatives to curb carbon emissions underscore the need for easily manufacturable, low-cost photovoltaic (PV) devices that can convert light into electrical energy. Composed of redox-active organic and organometallic dyes attached to semiconducting metal-oxide nanoparticle films, dye-sensitized solar cells (DSSCs)[1−3] are among the simplest, cheapest, and most easily tunable molecular PV devices that can perform this task by mimicking the light-harvesting mechanism of natural photosynthetic systems. Succinctly, the photogenerated excitons produced by chromophores dissociate into mobile electrons and holes, which traverse through oxide nanoparticles and electrolytes to opposite electrodes creating the requisite potential gradient to drive electrical current in the outer circuit. However, the limited dye-uptake capacity of metal-oxide nanoparticles restricts photon absorption and exciton population, which suppress short-circuit current (J_{SC}), whereas the random orientation and aggregation of dye molecules hinder charge separation and directional charge movement, which diminish their open-circuit voltage (V_{OC}). Together, these factors suppress the power conversion efficiency (PCE) of DSSCs and put them at a disadvantage to inorganic semiconductor-based solar cells, which benefit from superior light absorption and charge-transport capabilities of highly ordered crystalline materials. Therefore, to enhance the photovoltaic performance of molecular-based DSSCs, new strategies are needed to assemble and align a large number of electroactive chromophores on oxide surfaces that can absorb photons throughout the visible−near-infrared (NIR) region, produce adequate excitons and mobile charge carriers, support charge separation, movement and injection processes, and minimize charge recombination. To this end, we had previously demonstrated that coordinatively linked Zn-

Received: October 11, 2018
Accepted: December 25, 2018
Published: December 25, 2018

© 2018 American Chemical Society

DOI: 10.1021/acsami.8b17807
ACS Appl. Mater. Interfaces 2019, 11, 3196−3206

porphyrin···perylene[4] and Zn-phthalocyanine···perylene[5] dyads attached to TiO_2/fluorine-doped tin oxide (FTO) electrodes exhibited significantly greater photovoltaic response than individual chromophores owing to superior light absorption, charge separation, and directional electron-transport capabilities of the former.

Composed of metal cluster nodes linked by organic ligands, crystalline porous metal−organic frameworks (MOFs) have a unique capacity to amass and organize a large number of redox- and photoactive components (either as structural units or as encapsulated guests) in a highly ordered and periodic fashion.[6−8] Therefore, if incorporated properly in DSSCs, MOFs could not only prevent dye aggregation and charge recombination but also facilitate charge separation, movement, and injection processes in a way that transpires in crystalline inorganic semiconductor-based solar cells but hard to emulate in molecular PV devices. To realize these possibilities, in recent years, the focus of the MOF field has gravitated toward endowing them with electrical conductivity[9−16] and light-harvesting properties[17−21] by introducing redox- and photoactive building blocks[22−26] as well as guest molecules.[13−15,27,28] At the same time, the emergence of various film-growth techniques,[29] particularly the liquid-phase epitaxy (LPE) or layer-by-layer (LbL) method,[30−36] which yields oriented MOF thin films on self-assembled monolayer (SAM)-functionalized surfaces containing directing terminal groups, facilitated their integration into various electronic and photonic devices and vastly expanded their utility beyond traditional separation, storage, catalysis, and delivery applications.[6−8,37,38]

Marking the advances of the MOF field in recent years, at first, optically and redox-silent MOF thin films were employed in DSSCs as simple dye-loading materials to enhance the dye-loading capacity and prevent dye aggregation.[39,40] Although this strategy helped improve V_{OC} by impeding charge recombination, the insulating MOFs also hindered long-range charge movement and injection processes, diminishing the photocurrent density and overall efficiency of devices compared to those without MOFs.[41] The thin films of several traditional MOFs based on colorless aromatic ligands also displayed photovoltaic response upon iodine infiltration (PCE up to 1.2%),[42−47] but their inabilities to absorb visible−NIR light and generate photocurrents without iodine doping left the origin of photovoltaic behavior unclear and highlighted the need for intrinsically light-harvesting frameworks based on more powerful chromophores, such as porphyrin, perylene, and $Ru(bpy)_3^{2+}$ dyes.[48−63] Although the energy-transfer capability and catalytic activities of such light-harvesting MOFs have been widely explored,[51−57] their photovoltaic properties remained largely overlooked until lately[58−63] possibly because the latter also required properly oriented MOF films attached to electrode surfaces to support requisite charge separation, movement, and injection processes. Recently, Wöll,[58,59] Allendorf,[60] and others[61] have demonstrated that porphyrin-based MOFs could produce modest photocurrents under visible light (PCE: 0.0026−0.45%), whereas Morris et al.[62] demonstrated that $Ru(bpy)_3^{2+}$-based MOFs experienced slightly greater PCE than corresponding molecular $Ru(bpy)_3^{2+}$ complexes (~0.12 vs 0.08%). Chief among the factors that contributed to poor efficiencies of these MOF-sensitized solar cells included (i) the lack of proper electrical contact between the underlying electrodes and the drop-cast[60] and epitaxially grown MOF films on insulating SAMs,[58,59] which inhibited charge injection and (ii) inadequate exciton migration and charge-transport capabilities of three-dimensional (3D) porous frameworks, which suppressed the photocurrent density. The latter was explicitly demonstrated by Hupp et al.[63] using epitaxially grown [001]-oriented pillared porphyrin framework (PPF) films containing horizontally aligned porphyrin ligands, in which the photogenerated excitons could migrate only across 6−8 porphyrin layers separated by long pillars (~15 Å) but up to 9−11 layers when the interlayer gap was shrunk to ~7 Å in a two-dimensional (2D) framework via removal of the long pillar ligands. Recent studies of electrically conducting MOFs[9−16] also demonstrated that in-plane charge diffusion in 2D planar frameworks[9−11] is more facile and effective than delicately distance-dependent interplanar charge diffusion through π-stacked ligands[12] and ligand/guest stacks[13−16] in porous MOFs.

On the basis of these insights, we envisioned that properly oriented PPF films containing vertically aligned porphyrin layers that could support in-plane charge movement (electron hopping) along the porphyrin planes and inject them into underlying electrodes could be more effective for photovoltaic application than horizontally aligned porphyrin layers in a different film orientation that relied on a less effective interlayer (out-of-plane) charge movement.[63] Furthermore, although the LbL method reliably yields precisely oriented MOF films, it also requires thermally unstable insulating SAMs with directing terminal groups to dictate the direction of the film growth,[29−36] which cut off the electrical contact between MOFs and the underlying electrodes. Therefore, a new bottom-up protocol is necessary to grow such films directly on semiconducting oxide surfaces without any insulating SAMs. To this end, we[14] and others[43] have demonstrated that sintered ZnO films promote spontaneous solvothermal growth of uniform MOF films by covalently capturing carboxylate ligands on their surface. As described below, this technique turned out to be extremely effective for growing precisely [100]-oriented PPF-11 films featuring vertically aligned ZnTCPP layers directly on ZnO surfaces.

Herein, we report (i) spontaneous solvothermal growth of predominantly [100]-oriented PPF-11[50] films (Figure 1) featuring vertically aligned ZnTCPP struts and horizontal 2,2′-dimethyl-4,4′-bipyridine (DMBPY) pillars on ZnO−FTO electrodes, (ii) encapsulation of electron-deficient C_{60} guests inside PPF-11 and manifestation of ZnTCPP/C_{60} charge-transfer (CT) interaction in C_{60}-doped PPF-11 and (iii) an outstanding photovoltaic response of PPF-11/ZnO−FTO films in liquid-junction solar cells. We specifically selected noncatenated PPF-11 for this comprehensive study because its AA stacking pattern and uniformly large cavities (~17 × 17 × 14 Å^3) are suitable for fast electrolyte diffusion and infiltration of large C_{60} guests. Under simulated 1-sun illumination (AM 1.5), the devices made of [100]-oriented PPF-11/ZnO photoanodes, Pt/indium tin oxide (ITO) counter electrodes, and an I^-/I_3^- redox-couple-based electrolyte displayed excellent photovoltaic parameters (J_{SC} = 4.65 mA/cm^2, V_{OC} = 470 mV, and PCE = 0.86%) that easily surpassed all intrinsically light-harvesting 3D porous MOFs developed to date[58−62] as well as control devices made of bare ZnO, TCPP-coated ZnO, and drop-cast PPF-11 films by quite wide margins, i.e., with 10−1000 times higher J_{SC} and 2−375 times greater PCE. Furthermore, PPF-11 encapsulated electron-deficient C_{60} guests inside nearly half of their cavities and engaged them in CT interaction with electron-rich ZnTCPP

DOI: 10.1021/acsami.8b17807
ACS Appl. Mater. Interfaces 2019, 11, 3196−3206

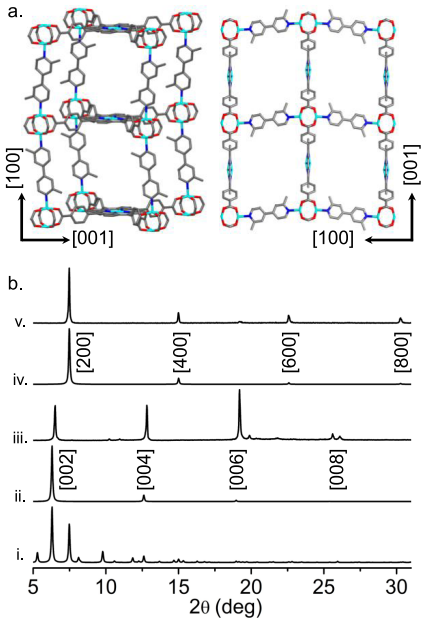

Figure 1. (a) Crystal structure of PPF-11 showing [100] and [001] planes. (b) The powder X-ray diffraction (PXRD) profiles of PPF-11: (i) simulated for bulk in random orientation, (ii) simulated for [001] orientation, (iii) observed for as-synthesized crystals, (iv) simulated for [100] orientation, (v) observed for solvothermally grown [100]-oriented films on ZnO surface.

ligands, leading to the emergence of characteristic CT absorption band and quenching of porphyrin photoluminescence. Although such host–guest CT interaction is known to enhance the electrical conductivity of doped frameworks,[14−16] the C_{60}-doped PPF-11/ZnO films displayed no measurable conductivity surge and much weaker photovoltaic response (PCE ∼ 0.1%) compared to undoped PPF-11 films, possibly due to occlusion of electrolytes from the C_{60}-occupied cavities and poor charge-transport and injection capabilities of isolated C_{60} guests.

RESULTS AND DISCUSSION

Bulk PPF-11 [Zn_2(ZnTCPP)(DMBPY)] Synthesis and Characterization. Bulk PPF-11 (Figure 1a) was synthesized solvothermally by heating a solution of $Zn(NO_3)_2·6H_2O$ (90 mg, 0.3 mmol), TCPP (80 mg, 0.1 mmol), DMBPY (38 mg, 0.2 mmol), and 1 M HNO_3/EtOH (0.2 mL) in dimethylformamide (DMF)/EtOH (3:1, 20 mL) at 80 °C for 24 h.[50] The resulting reddish purple colored, rectangular plate-shaped crystals were washed thoroughly with fresh DMF to remove unreacted precursors before characterization. The powder X-ray diffraction (PXRD) pattern of as-synthesized crystals displayed (Figure 1b) low-angle diffraction peaks (2θ = 6.3, 12.6, 18.9°) that matched perfectly with the simulated diffraction pattern of PPF-11 along [001] direction, revealing spontaneous growth of the bulk material along that direction. This observation was consistent with other PPFs, which also displayed preferred orientation along certain directions when no special technique was used to average their orientations.[49] Like other PPFs, the PXRD profile of extensively ground PPF-11 powder displayed diminished crystallinity instead of just random orientation. In PPF-11,[50] the ZnTCPP struts are located in the crystallographic *ab* planes and form Zn_2 paddlewheel nodes, which are connected by axially coordinated DMBPY pillars located along the *c*-axis. Unlike BPY, DMBPY pillars coordinated exclusively with the Zn_2 nodes (not with the ZnTCPP centers), creating an AA stacking pattern and uniformly large cavities in PPF-11 that are suitable for electrolyte diffusion and C_{60} encapsulation.

Spontaneous Solvothermal Growth of [100]-Oriented PPF-11 Films on ZnO–FTO Substrates. To grow PPF-11 films directly on semiconducting metal-oxide-coated electrodes without an insulating SAM that could impede charge injection, we adopted a bottom-up protocol[14] developed previously in our laboratory using annealed ZnO/

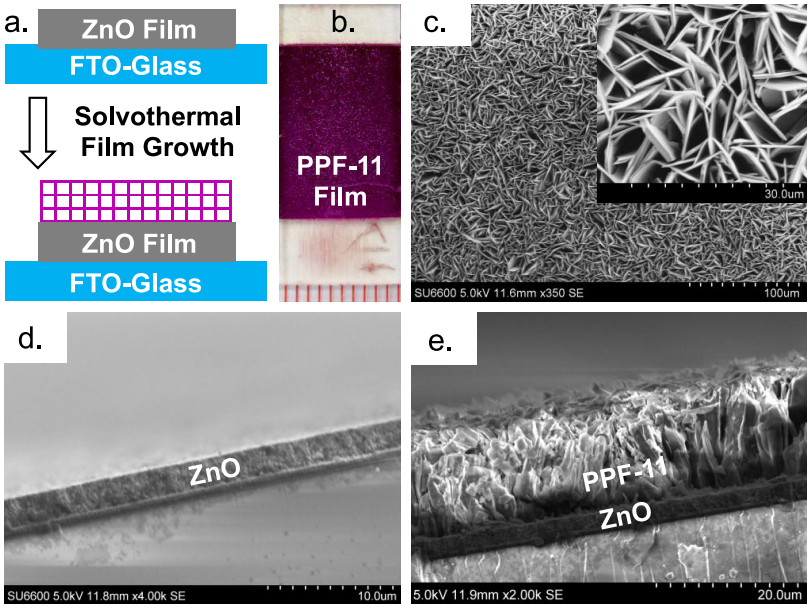

Figure 2. (a) Schematic diagram outlining the solvothermal growth of PPF-11 film. (b) A photograph of solvothermally grown PPF-11/ZnO film. (c) Scanning electron microscopy (SEM) images of PPF-11/ZnO film showing densely packed crystals aligned uniformly on the surface. Cross-sectional-SEM images of (d) 2.5 μm thick annealed ZnO film and (e) solvothermally grown 10 μm thick PPF-11 film on ZnO layer.

DOI: 10.1021/acsami.8b17807
ACS Appl. Mater. Interfaces 2019, 11, 3196−3206

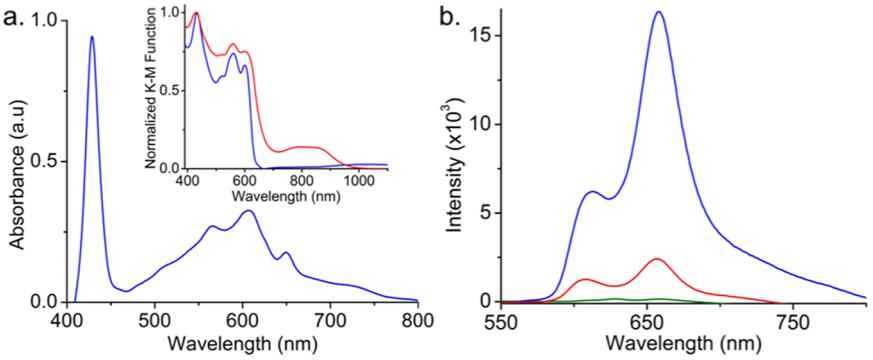

Figure 3. (a) UV−vis spectrum of [100]-oriented PPF-11/ZnO films. Inset: diffuse reflectance spectra of PPF-11 (blue) and C_{60}-doped PPF-11 (red). (b) The photoluminescence spectra of PPF-11 (blue), C_{60}-doped PPF-11 (red), and free ZnTCPP (green) showing significant fluorescence amplification in the MOF.

FTO substrates, which prompted spontaneous growth of uniform MOF films on ZnO surfaces under solvothermal conditions. Although TiO_2-coated FTO electrodes are used more commonly in DSSCs, in our experience, under solvothermal conditions, MOF films did not grow as uniformly and reliably on TiO_2 surfaces as they did on ZnO. From the device performance and relative energy standpoints, the use of ZnO instead of TiO_2 was not an issue at all because both are n-type semiconductors with comparable conduction band energies (ca. −4.4 eV) and electronic band gaps (3.4−3.7 eV) that are amenable to electron transfer from photosensitized PPF-11 (lowest unoccupied molecular orbital (LUMO): −3.1 eV) and subsequent electron injection into FTO conduction band (−4.7 eV).[64,65] The large overpotentials (∼1.3 eV) for photoinduced electron transfer from PPFs to either metal-oxide could hinder charge injection and promote charge recombination making devices less efficient. However, on the basis of density functional theory (DFT) calculations, Wöll et al.[58] proposed that porphyrin-based MOFs have indirect band gaps that could facilitate charge injection into underlying electrodes despite large overpotentials.

Optically transparent ZnO-coated FTO electrodes were prepared by spin-coating FTO substrates with ZnO/EtOH suspension, followed by sintering at 350 °C for 30 min.[14] To grow PPF-11 films under solvothermal conditions, first the nucleation of MOF crystals was initiated by heating DMF/EtOH (3:1 mL) solutions of $Zn(NO_3)_2{\cdot}6H_2O$ (0.03 mmol), TCPP (0.01 mmol), DMBPY (0.02 mmol), and 1 M HNO_3/EtOH (20 μL) in screw-capped vials at 80 °C for 2 h. Then, annealed ZnO−FTO slides were immersed into these precursor solutions at upright positions and stood at 80 °C for 30 min, which led to spontaneous formation of bright purple colored uniform crystalline films selectively on the ZnO-coated areas (Figure 2). After washing these films extensively with DMF (soaked for 3 days, solvent refreshed twice a day), they were stored in various organic solvents, such as DMF, acetonitrile, propylene carbonate, or toluene, where they remained intact for months without any delamination or dissolution. The PXRD analysis demonstrated that these films were composed of PPF-11 crystals oriented along the [100] plane, i.e., the ZnTCPP struts forming the Zn_2 nodes stood vertically, whereas DMBPY pillars bridging the nodes lied horizontally on the underlying ZnO surface, as the observed peaks ($2\theta \approx 7.5$, 15, 22.5, and 30°) matched perfectly with those simulated for PPF-11 along [100] direction (Figure 1b). Furthermore, the ^{1}H NMR spectra of digested (in DMSO-d_6 (0.5 mL) containing a small drop of CF_3CO_2D) bulk PPF-11 crystals and crystalline MOFs scraped off from the films displayed characteristic signals of TCPP and DMBPY ligands at 1:1 ratio (Figure S1), unequivocally confirming that both were indeed the same material [Zn_2(ZnTCPP)(DMBPY)] (note: different PPFs have distinct TCPP-to-pillar ratios and only PPF-11 has a 1:1 ratio).

No PPF-11 film was formed on the ZnO-free areas of FTO slides, and the [100] orientation of solvothermally grown PPF-11/ZnO films was totally different from that of preferential [001] orientation of bulk crystals formed under the same conditions, indicating that ZnO surface not only facilitated the film formation by first capturing the TCPP struts through COOH groups but also guided the direction of film growth by aligning them vertically on the surface. The ZnO-bound vertical TCPP ligands then formed $Zn_2(COO)_4$ paddle-wheel nodes, which were axially connected by DMBPY pillars leading to layer-by-layer bottom-up growth of PPF-11 crystals along the [100] plane. Although bare ZnO films consistently yielded precisely [100] oriented PPF-11 films, to maximize the directing effect of ZnO-bound TCPP ligands and also maintain the proper stoichiometry of all precursors during solvothermal film growth, the ZnO−FTO substrates were first soaked in TCPP solutions at room temperature for 15 h. to allow these ligands to first anchor on the surface and form a monolayer. The resulting translucent pink TCPP-coated ZnO films were washed thoroughly to remove any physisorbed ligands and subsequently used to grow PPF-11 films under the same solvothermal conditions described above. The PPF-11 films grown on TCPP-precoated ZnO surface were even more uniform and robust than those formed on unmodified ZnO films via in situ anchoring of TCPP ligands during solvothermal film growth. Nevertheless, the PPF-11 films grown on TCPP-precoated and unmodified ZnO substrates displayed identical PXRD patterns, confirming that they both had the same [100] orientation. Interestingly, the preferred [100] orientation of solvothermally grown noncatenated PPF-11 films on unmodified and TCPP-precoated ZnO surfaces differed from the preferred [001], [110], and [111] orientations of solvothermally grown catenated PPF-5 films on dihydroxybenzioic acid-modified TiO_2 substrates,[30] suggesting that the covalently anchored TCPP monolayers on ZnO surface dictated the orientation of our PPF-11 films. We envisioned that the vertically aligned ZnTCPP multilayers in [100]-oriented PPF-11/ZnO films should foster in-plane charge movement, whereas the covalently anchored TCPP

DOI: 10.1021/acsami.8b17807
ACS Appl. Mater. Interfaces 2019, 11, 3196−3206

ligands should facilitate charge injection into underlying ZnO/FTO electrode, and their combined effects should lead to superior photovoltaic behavior of these films than only TCPP-coated ZnO and not covalently bound drop-cast PPF-11 films with a different ([001]) orientation.

The scanning electron microscopy (SEM) images of PPF-11 films revealed (Figure 2c–e) densely packed rectangular slablike crystals aligned vertically on the surface. The cross-sectional SEM (cs-SEM) images revealed a ca. 10 μm thick crystalline PPF-11 layer (grown solvothermally for 30 min) on top of a 2.5 μm thick ZnO layer. No PPF-11 crystal was found embedded within the annealed ZnO layer. Both PPF-11 and ZnO layers were uniform across the films. These PPF-11/ZnO films were mechanically robust and exhibited the characteristic PXRD pattern and SEM images even after prolonged exposure to ambient conditions. After carefully removing the PPF-11 film from the ZnO surface (scraped off with the edge of a weighing paper and washed with a steam of CH_2Cl_2), the re-exposed ZnO substrate displayed only the characteristic PXRD signals of ZnO and FTO at 2θ = 25–40° but no characteristic PPF-11 signal at lower angles (Figure S2), confirming that PPF-11 films grew only on top of the ZnO layer, not within. Furthermore, the SEM images of bare ZnO films also revealed that these substrates remained intact after being exposed to solvothermal reaction conditions (Figure S3). Shorter film-growth time (≤15 min) yielded thinner, less uniform films, whereas longer growth time and more concentrated precursor solutions produced thicker films, which were prone to delaminate from ZnO substrates yielding free-standing PPF-11 membranes.

Optical Properties of PPF-11. The UV–vis spectrum of PPF-11 films (Figure 3a) displayed characteristic Soret band (430 nm) and Q-bands (566, 607, and 650 nm) of porphyrin ligands. The presence of more than two Q-bands suggested that some free-base porphyrins were also present since PPF-11 films were grown on TCPP-coated ZnO films. From the onset of the longest wavelength absorption peak (670 nm), the optical band gap (~1.9 eV) was calculated. The steady-state emission studies (Figure 3b) showed that upon 432 nm excitation (the Soret band of ZnTCPP), PPF-11 displayed two strong emission peaks at 610 and 660 nm corresponding to porphyrin emission, which were ca. 10^3 times higher in intensity compared to those of free ZnTCPP ligands.[60] The fluorescence amplification of PPF-11 can be attributed to rigidification and well-defined spacing of ZnTCPP ligands inside the framework, which restricted their rotational and vibrational motions and prevented self-quenching.[19]

Electronic Properties of PPF-11. The cyclic voltammogram of PPF-11/ZnO films displayed (Figure S4) a quasireversible peak at +1.05 V (vs Ag/AgCl) corresponding to ZnTCPP oxidation. From the onset of this oxidation peak (0.6 V) and band gap (1.9 eV), the highest occupied molecular orbital (HOMO, −5.0 eV) and LUMO (−3.1 eV) levels of PPF-11 were estimated.[4,5] These experimental HOMO/LUMO levels of PPF-11 were in good agreement with the calculated values (DFT/HSE06) of an analogous PPF-4 containing the same ZnTCPP struts.[60] The relative energies of the LUMO of PPF-11 and the conduction band edge of ZnO (−4.4 eV) are amenable to electron transfer from photosensitized PPF-11 films to the underlying ZnO layer (Figure 4). Similarly, the HOMO levels of PPF-11 films and I^-/I_3^- redox couple (−4.8 eV) are suitable for hole transfer from photo-oxidized ZnTCPP struts to the electrolyte. DFT

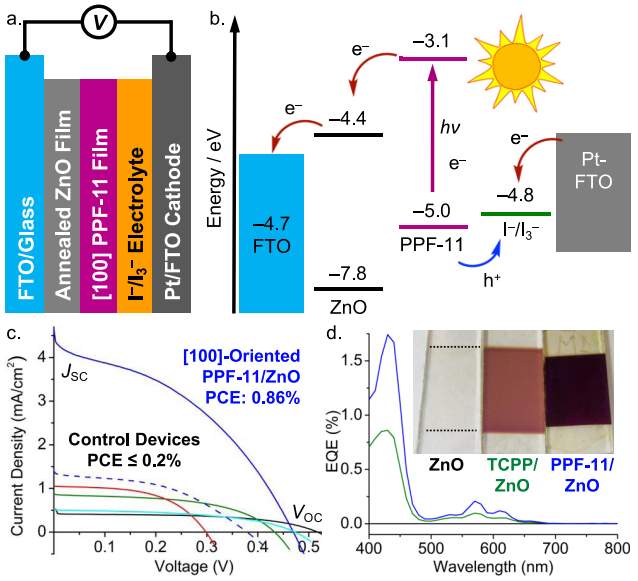

Figure 4. (a) Device architecture of a MOF-sensitized solar cell based on PPF-11/ZnO–FTO photoanode, Pt-FTO counter electrode, and I^-/I_3^- electrolyte. (b) A simplified energy-level diagram depicting the relative HOMO, LUMO, and conduction bands of different components and the putative photoinduced electron-transfer pathway. (c) The J–V plots of devices containing [100]-oriented PPF-11/ZnO film (solid blue), drop-cast PPF-11 on TCPP-coated ZnO (dashed blue), drop-cast PPF-11 on bare ZnO (cyan), C_{60}-doped [100]-oriented PPF-11/ZnO film (red), TCPP-coated ZnO films (green), and bare ZnO film (black) showing their photovoltaic behavior under 1-sun illumination. (d) The external quantum efficiency (EQE) spectra of [100]-oriented PPF-11/ZnO (blue), TCPP/ZnO (green), and blank ZnO films showing the photovoltaic response of each device as a function of irradiation wavelength. Inset: photographs of corresponding films used as photoanodes.

calculations by Wöll et al.[58] predicted that porphyrin-based MOFs have indirect band gaps, which could facilitate electron injection from these frameworks to underlying electrode despite having large overpotentials.

Doping PPF-11 with Electron-Accepting C_{60} Guests. To explore electron-/energy-transfer capability of PPF-11, we doped it with a strong electron-acceptor C_{60} (LUMO: −4.2 eV) by soaking PPF-11 crystals and films in saturated C_{60} solutions in toluene at 60 °C for 7 days. The externally adhered C_{60} molecules were removed by washing them with fresh toluene (3 × 5 mL, ~10 s each time). After C_{60} infiltration, the bright purple colored PPF-11 crystals and films turned dark violet. The amount of encapsulated C_{60} molecules in PPF-11 was determined by extracting them out by soaking a known amount of C_{60}-doped PPF-11 in hot toluene (refreshed every 12 h) until the washing solution became completely colorless and did not display any C_{60} absorption peak. The UV–vis analysis of the combined washing solutions revealed that 2.9 mg of C_{60} was encapsulated in 9.5 mg of C_{60}-doped PPF-11. Taking [Zn_2(ZnTCPP)-(DMBPY)] as the molecular formula of activated PPF-11, we estimated that the ZnTCPP/C_{60} ratio was 2:1, i.e., roughly half of the PPF-11 cavities, presumably, the alternate ones, were occupied by guest C_{60} molecules. In other words, the encapsulated C_{60} population inside the doped PPF-11 was not enough to fill all of the cavities and form continuous π-stacks.

DOI: 10.1021/acsami.8b17807
ACS Appl. Mater. Interfaces 2019, 11, 3196–3206

Table 1. Photovoltaic Parameters of DSSCs Made of Undoped and C_{60}-Doped [100]-Oriented PPF-11/ZnO Films and Control Devices Made of TCPP-Coated and Bare ZnO Films under Simulated 1-sun Illumination

photoanode	J_{SC} (mA/cm^2)	V_{OC} (mV)	FF (%)	PCE (%)
[100]-oriented PPF-11/ZnO−FTO	4.20 ± 0.50	470 ± 2	41 ± 4	0.82 ± 0.05
drop-cast PPF-11 on TCPP/ZnO−FTO	1.17 ± 0.16	403 ± 22	50 ± 4	0.23 ± 0.01
TCPP/ZnO−FTO	1.22 ± 0.32	424 ± 23	48 ± 4	0.24 ± 0.04
drop-cast PPF-11 on ZnO−FTO	0.65 ± 0.11	459 ± 17	51 ± 6	0.15 ± 0.03
ZnO−FTO	0.62 ± 0.10	530 ± 20	54 ± 1	0.17 ± 0.02
C_{60}-doped PPF-11/ZnO−FTO	0.67 ± 0.30	335 ± 32	59 ± 5	0.13 ± 0.04

The Brunauer−Emmett−Teller surface area of PPF-11 measured from CO_2 sorption decreased from 7.3 to 6 m^2/g upon C_{60} infiltration (Figure S5). The relatively low surface area of undoped PPF-11 could be attributed to collapse of activated framework since we did not use the supercritical CO_2-based activation method.[50] As observed with another C_{60}-doped MOF,[16] the PXRD pattern of PPF-11 remained mostly unchanged upon C_{60} infiltration (Figure S6), indicating that the structure and crystallinity of the framework remained largely intact. The appearance of a few new peaks in the C_{60}-doped PPF-11 could be attributed to partial disruption of the original orientation of the framework. The thermogravimetric analysis (TGA) revealed that (Figure S7) undoped PPF-11 gradually lost ca. 25% weight between 25 and 375 °C, whereas C_{60}-doped PPF-11 lost only 10% of initial weight in the same temperature range, suggesting that the presence of spherical C_{60} guest molecules made them less prone to collapse and gradual weight loss during rising temperature. The concomitant differential scanning calorimetry analysis revealed that neither undoped nor C_{60}-doped PPF-11 underwent any phase transitions until ca. 400 °C, i.e., both materials were thermally stable.

Optical and Electronic Properties of C_{60}-Doped PPF-11. In addition to characteristic Soret and Q-bands of porphyrin ligands, the diffuse reflectance spectrum of C_{60}-doped PPF-11 also displayed a broad CT band at 650−930 nm region (Figure 3a inset), revealing that the electron-rich ZnTCPP ligands and the electron-deficient C_{60} guests were involved in significant CT interactions.[16] The onset of the CT band (930 nm) in C_{60}-doped PPF-11 corresponded to an optical band gap of 1.3 eV, which was ∼0.6 eV narrower than that of undoped PPF-11 (vide supra). Furthermore, the photoluminescence intensity of C_{60}-doped PPF-11 diminished significantly from that of the undoped material (Figure 3b), as the ZnTCPP/C_{60} CT interaction quenched the porphyrin emission.[66]

Photovoltaic Performance of [100]-Oriented PPF-11/ZnO Films. Finally, to investigate the light-harvesting capability and photovoltaic performance of PPF-11, we fabricated liquid-junction solar cells (Figure 4a) using [100]-oriented PPF-11 films grown on TCPP-coated ZnO−FTO slides (30 min growth, 10 μm thick) as photoanode, Pt-FTO counter electrode, and an I^-/I_3^- redox-couple-based electrolyte in propylene carbonate, a highly polar, nonvolatile, and noncoordinating solvent. As described earlier, the HOMO and LUMO energy levels of PPF-11 and I^-/I_3^- redox couple and the conduction band energies of ZnO and FTO are amenable to cascade photoinduced electron-transfer pathway depicted in the simplified energy-level diagram (Figure 4b). To determine the actual roles and benefits of covalently attached [100]-oriented PPF-11/ZnO films, they were compared with control devices made of bare ZnO- and TCPP-coated ZnO films as well as drop-cast films of PPF-11 crystals on bare ZnO- and TCPP-coated ZnO−FTO slides, which displayed a preferential [001] orientation in PXRD similar to as-synthesized PPF-11. The C_{60}-doped [100]-oriented PPF-11 films were used to investigate how the ZnTCPP/C_{60} CT interaction influenced their light-harvesting behavior. In all these devices (three of each type), the photoactive area was kept constant at 0.2 cm^2 (0.5 × 0.4 cm^2). The photoanodes and Pt-FTO cathodes were separated by a thermally fused insulating surlyn film sandwiched between the two electrodes surrounding the photoactive areas at the center. The photovoltaic response and photoconversion efficiencies of these devices were determined from current−voltage (J−V) plots (Figure 4c) and the charge-transfer resistance at electrode/electrolyte interfaces from electrochemical impedance spectra (EIS) recorded under simulated 1-sun illumination (AM 1.5, 100 mW/cm^2 light intensity).

Under AM 1.5 illumination, the solvothermally grown [100]-oriented PPF-11/ZnO−FTO films displayed excellent photovoltaic response (J_{SC} ≈ 4.65 mA/cm^2, V_{OC} ≈ 470 mV, fill-factor ≈ 40%, and PCE ≈ 0.86%), which surpassed the photovoltaic parameters of all control devices made of bare ZnO, TCPP-coated ZnO, and drop-cast PPF-11 films on bare ZnO and TCPP-coated ZnO−FTO electrodes by wide margins (Tables 1 and S1). For example, the [100]-oriented PPF-11/ZnO films displayed ca. 5 times greater J_{SC} and 4 times higher PCE than just TCPP-coated ZnO films. The superior photovoltaic performance of the former can be attributed to the fact that it contained much greater number of vertically aligned ZnTCPP chromophores, which could absorb more photons than just TCPP monolayers present in the latter and thereby generate more excitons and mobile charge carriers (electrons and holes) giving rise to higher J_{SC} and PCE. Furthermore, the [100]-oriented PPF-11/ZnO films also displayed 3−4 times greater J_{SC} and PCE than drop-cast PPF-11 films with predominantly [001] orientation, revealing that the proper orientation and covalent attachment of light-harvesting MOFs to the underlying electrode surfaces play important roles on their photovoltaic performances. The superior photovoltaic response of [100]-oriented PPF-11/ZnO could be attributed to a more facile in-plane charge movement through the vertically oriented ZnTCPP planes since out-of-plane interlayer exciton diffusion in [001]-oriented PPF films was known to be limited to only a few horizontal porphyrin layers.[63] The diffusion of electrolyte could also be different in differently oriented PPF films. Furthermore, the better charge-injection capability of covalently attached [100]-oriented PPF-11/ZnO films than drop-cast films was also evident from a smaller interfacial charge-transport resistance measured by electrochemical impedance spectroscopy (vide infra). The drop-cast PPF-11 films on bare ZnO- and TCPP-coated ZnO films displayed similar photovoltaic parameters as those of

DOI: 10.1021/acsami.8b17807
ACS Appl. Mater. Interfaces 2019, 11, 3196−3206

Table 2. Charge-Transfer Resistance (Ohm) of Different DSSCs at the Photoanode/Electrolyte Interfaces Obtained from EIS Measurements Conducted under Simulated 1-sun Illumination

photoanode composition	R_S	R_1	R_2
[100]-oriented PPF-11/ZnO film	46 ± 1	159 ± 2	224 ± 34
drop-cast PPF-11 on TCPP/ZnO−FTO	39 ± 6	178 ± 1	509 ± 26
TCPP/ZnO−FTO	27 ± 2	220 ± 9	431 ± 11
ZnO−FTO	47 ± 5	116 ± 13	754 ± 13
C_{60}-doped PPF-11/ZnO−FTO	39 ± 2	305 ± 8	492 ± 7

blank ZnO and TCPP/ZnO films, respectively, indicating that the drop-cast PPF-11 films played little, if any, role in photocurrent generation, as they lacked the requisite charge separation, transport, and injection capabilities.

More importantly, the [100]-oriented PPF-11/ZnO films also outperformed all existing visible light-harvesting 3D porous MOF-sensitized solar cells, including a solid-state device based on a Zn-porphyrin-based LbL MOF films on FTO electrode (J_{SC} = 23.4 μA/cm^2, V_{OC} = 267 mV, and PCE = 0.017%),[58] a Pd-porphyrin-based LbL MOF film on SAMs-coated FTO electrode (J_{SC} = 0.71 mA/cm^2, V_{OC} = 700 mV, and PCE = 0.45%),[59] drop-cast PPF-4 films on TiO_2/ITO electrode (J_{SC} = 8.5 μA/cm^2, V_{OC} = 515 mV, and PCE = 0.0023%),[60] and solvothermally grown $Ru(bpy)_3^{2+}$-based Zr-MOF films on TiO_2/FTO electrodes (J_{SC} = 0.45 mA/cm^2, V_{OC} = 480 mV, and PCE = 0.125%)[62] by quite wide margins, i.e., with 10−1000 times greater J_{SC} and 2−375 times higher PCE. The superior photovoltaic performance of [100]-oriented PPF-11 films covalently attached to ZnO/FTO surfaces could be attributed to several putative factors, including their potentials to (i) absorb more photons and generate more excitons and mobile charge carriers than chromophore monolayers and epitaxially grown MOF thin films containing much fewer chromophores, (ii) facilitate charge separation, (iii) support in-plane charge movement across the film through the vertically aligned multilayers of ZnTCPP chromophores linked by Zn_2 nodes, and (iv) inject photogenerated electrons into the underlying ZnO layer through covalently anchored TCPP ligands. Although it was difficult to pinpoint to any specific reason, it is worth noting that all these factors are feasible in [100]-oriented PPF-11/ZnO films and could potentially contribute to their superior photovoltaic performance. In particular, the facile charge-transport and injection capabilities of [100]-oriented PPF-11/ZnO photoanode was evident from its lower interfacial charge-transfer resistance than other devices (vide infra).

To demonstrate that the [100]-oriented PPF-11/ZnO films were indeed responsible for photocurrent generation due to photon absorption by porphyrin chromophores, we measured the external quantum efficiency (EQE) of our devices as a function of visible wavelength (Figure 4d). The EQE profiles of both PPF-11/ZnO films and TCPP-coated ZnO films essentially resembled the porphyrin absorption spectrum (Figure 3a), i.e., the photocurrent was produced at porphyrin's Soret and Q-bands. Consistent with the J−V plots measured under 1-sun illumination, the [100]-oriented PPF-11/ZnO films registered a higher EQE than TCPP/ZnO films throughout the visible region. In contrast, the EQE of bare ZnO−FTO films was negligible, as it hardly absorbed any visible light or produced any measurable photocurrent in this region. These results unequivocally confirmed that the ZnTCPP ligands in PPF-11 were indeed responsible for photocurrent generation.

Since C_{60}-doped PPF-11 experienced significant ZnTCPP/C_{60} CT interaction and narrower optical band gap than undoped PPF-11, we initially anticipated that it could potentially display a stronger photovoltaic response. Surprisingly though, the C_{60}-doped [100]-oriented PPF-11 films displayed much weaker photovoltaic response (J_{SC} = 1.05 mA/cm^2, V_{OC} = 298 mV, and PCE = 0.17%) than undoped films (Table 1), indicating that the encapsulated C_{60} molecules failed to promote long-range electron movement in PPF-11 and may have actually hindered these processes. One potential reason for such muted photovoltaic response of C_{60}-doped PPF-11 films could be the exclusion of hole-transporting I^-/I_3^- redox couple from the C_{60}-occupied PPF-11 cavities. Furthermore, since only half of the PPF-11 cavities were filled with C_{60} (based on the amount of encapsulated C_{60} in doped PPF-11, vide supra), only isolated ZnTCPP/C_{60} CT complexes instead of continuous π-stacks were formed. Since C_{60} is an excellent electron acceptor but a poor charge conductor, the isolated CT complexes could not support long-range charge movement and instead may have facilitated charge recombination due to the proximity of electron-donor and -acceptor units.

To further rationalize the distinct photovoltaic performances of all these PV devices, the charge-transfer resistances (R_{CT}) at each electrode/electrolyte interface was measured through electrochemical impedance spectroscopy over a frequency range of 10^5−10^{-1} Hz under 1-sun illumination and dark immediately after PV measurements (Supporting Information). The interfacial charge-transfer resistances (Table 2) were obtained by fitting the Nyquist plots (Figures 5 and S8) obtained from EIS analysis to an apropriate equivalent circuit model[44−47,60,67−69] (Figure 5a inset) consisting of two parallel RC circuits (R_1/Q_1 and R_2/Q_2) connected in series with a

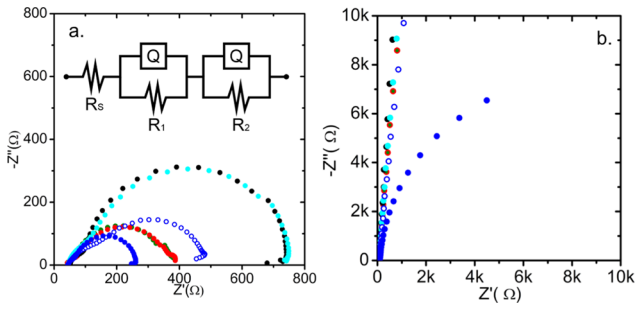

Figure 5. Electrochemical impedance spectra (EIS) of [100]-oriented PPF-11/ZnO−FTO (solid blue circle), drop-cast PPF-11 on TCPP/ZnO (blue open circles), drop-cast PPF on ZnO (cyan), C_{60}-doped PPF-11/ZnO−FTO (red), TCPP/ZnO (green), and bare ZnO (black) films measured (a) under simulated 1-sun illumination and (b) dark at open-circuit condition. Inset (a): the equivalent circuit model of our devices to which the EIS data were fit to derive the interfacial charge-transfer resistances.

DOI: 10.1021/acsami.8b17807
ACS Appl. Mater. Interfaces 2019, 11, 3196−3206

series resistance (R_S), where R_1 and R_2 represented the charge-transfer resistance at Pt/electrolyte and photoanode/electrolyte interfaces, respectively, the constant phase elements Q_1 and Q_2 corresponded to chemical capacitance of respective electrode/electrolyte interface, and R_S denoted the combined resistance of FTO substrate, ZnO, and electrolyte.[68] Each Nyquist plot displayed two prominent semicircles: (i) the high-frequency (100−1000 Hz) small semicircle at lower Z' value was assigned to R_1 at Pt/electrolyte interface and (ii) the intermediate-frequency (10−100 Hz) large semicircle to R_2 at the photoanode/electrolyte interface. The smaller the semicircle, the lower was the corresponding interfacial charge-transfer resistance. R_S corresponded to the high-frequency x-axis intercept of the first (left) semicircle. While the first two semicircles were clearly visible in the Nyquist plots of all our devices, a third low-frequency (mHz to 10 Hz) semicircle associated with electrolyte diffusion was typically indistinguishable in most MOF-based solar cells,[44−47,67] including ours. A low-frequency loop was observed in some of these devices (Figures 5a and S8), which could be attributed to inductance caused by adsorption of electrolyte at the electrode.[70] Although the low-frequency inductance tail has been observed occasionally in DSSCs,[69] its rather small contribution is often ignored especially when the main focus of the work rests on the photoanode materials (R_2).

Among these parameters, there were little variations in R_S values of different devices because they all contained the same FTO, ZnO, and electrolyte. The R_1 values of different devices varied to some extent possibly because of slightly different morphologies of Pt/FTO electrodes used in each cell and different regeneration rates of redox couples at the Pt/electrolyte interface depending on the photoanodes.[47] Similar variations of R_1 values have also been observed in other MOF-based solar cells.[47] The largest and most significant variations were observed in R_2 values associated with charge-transfer resistance at the all-important photoanode/electrolyte interfaces. Under 1-sun illumination, the [100]-oriented PPF-11/TCPP-ZnO films displayed the smallest R_2 value (224 Ω), which was significantly lower than that of drop-cast PPF-11 on TCPP-ZnO (509 Ω), TCPP-ZnO (431 Ω), and bare ZnO films (754 Ω), indicating that the oriented PPF-11 film covalently attached to the underlying ZnO substrate facilitated the most efficient electron transport. The much larger R_2 value of C_{60}-doped PPF-11/ZnO films (492 Ω) also indicated a less facile charge movement through this photoanode possibly because of exclusion of I^-/I_3^- electrolyte from the C_{60}-occupied cavities. Furthermore, the Nyquist plot of C_{60}-doped PPF-11/ZnO films also displayed a third low-frequency (mHz to Hz) semicircle corresponding to electrolyte diffusion, which was invisible/indistinguishable in other devices, suggesting that the presence of C_{60} guests inside PPF-11 cavities hindered electrolyte diffusion. The involvement of this additional resistance possibly diminished its photovoltaic performance. Thus, the EIS results were fully consistent with the trend of photovoltaic performances of different photoanodes (Table 1), revealing how the charge-transfer resistance (R_2) at different photoanode/electrolyte interfaces influenced the photovoltaic parameters of the devices.

In the absence of light, all these devices displayed (Figure 5b) much larger interfacial charge-transfer resistances (>10^4 Ω) under open-circuit conditions. Among all these devices, the [100]-oriented PPF-11/TCPP-ZnO films displayed the smallest resistance, suggesting that they enjoyed the highest intrinsic electrical conductivity. However, upon simulated 1-sun illumination, the R_2 values of these devices decreased (~10^2 Ω) commensurately with their respective photovoltaic response reflected in $J-V$ plots.

CONCLUSIONS

In summary, this work demonstrated a rare, if not unprecedented, spontaneous solvothermal growth and outstanding photovoltaic performance of precisely [100]-oriented, uniform PPF-11 films attached to annealed ZnO−FTO surfaces featuring vertically aligned ZnTCPP multilayers connected by $Zn_2(COO)_4$ paddle-wheel nodes. The covalently anchored TCPP ligands on ZnO surface dictated the direction of PPF-11 film growth under solvothermal conditions, eliminating the need for electrically insulating and thermally unstable SAMs used in LbL or LPE methods to control the orientation of MOF thin films. PPF-11 displayed significant fluorescence amplification compared to free ZnTCPP due to ligand rigidification inside the framework. The noncatenated PPF-11 was able to encapsulate large electron-deficient C_{60} guests inside its cavities and engaged them in ZnTCPP/C_{60} CT interaction, which was evident from characteristic CT absorption band and photoluminescence quenching of the framework.

Acting as photoanodes in liquid-junction solar cells, the [100]-oriented PPF-11/ZnO−FTO films displayed much superior photovoltaic performances, i.e., 10−1000 times greater J_{SC} and 2−375 times higher PCE than all control devices made of bare ZnO, TCPP-coated ZnO, and drop-cast PPF-11 films on bare and TCPP-coated ZnO−FTO slides as well as all previously reported intrinsically light-harvesting porphyrin and $Ru(bpy)_3^{2+}$-based MOF-based solar cells.[58−62] The stronger photovoltaic response of the former could be attributed to a number of factors, including (i) more photon absorption and exciton formation capabilities of ZnTCPP multilayers, (ii) more facile in-plane charge movement through vertically aligned ZnTCPP planes, and (iii) better interfacial charge-transport and injection capabilities of covalently anchored PPF-11 films. Although it was difficult to delineate the contributions of these possibilities from experimental results, the positive effects of [100] orientation and covalent attachment of PPF-11 films were clearly evident from their much higher J_{SC} and PCE and lower interfacial charge-transport resistance than drop-cast PPF-11 films with a totally different orientation (predominantly [001]) and without covalent attachment to ZnO surface. Despite experiencing significant ZnTCPP/C_{60} charge-transfer interaction and narrower optical band gap, the C_{60}-doped PPF-11/ZnO films showed much weaker photovoltaic response than undoped PPF-11 films possibly because of the exclusion of I^-/I_3^- electrolyte from the C_{60}-occupied cavities and the inability of isolated C_{60} molecules to support long-range electron transfer. Although PCE of our [100]-oriented PPF-11/ZnO films fell just short of 1%, to our knowledge, only a solid-state PV device made of Co^{II}-bridged viologen multilayers, i.e., a linear coordination polymer, not a 3D porous MOF, was known to display a greater photovoltaic response.[67] More importantly, our comprehensive studies and foregoing discussions revealed the key structural and functional criteria for light-harvesting capability of MOFs and charted a new blueprint for improving the efficiency of MOF-sensitized solar cells. For instance, a second electroactive chromophore could be introduced in PPFs as pillars and conducting polymer as guests to expand

DOI: 10.1021/acsami.8b17807
ACS Appl. Mater. Interfaces 2019, 11, 3196−3206

their light-absorption range and promote charge separation and transport, respectively. Realizing these tantalizing potentials is a focus of our ongoing investigations.

■ ASSOCIATED CONTENT

Supporting Information

The Supporting Information is available free of charge on the ACS Publications website at DOI: 10.1021/acsami.8b17807.

Experimental details, PPF-11 synthesis, C_{60}-doping, solvothermal film growth, device construction, table containing photovoltaic parameters of three devices of each type, ^{1}H NMR, SEM, cyclic voltammogram, CO_2 sorption isotherms, PXRD, EIS, and TGA data (PDF)

■ AUTHOR INFORMATION

Corresponding Author

*E-mail: souravs@clemson.edu.

ORCID

Sourav Saha: 0000-0001-6610-4820

Author Contributions

†M.A.G. and D.K.P. contributed equally to this work.

Notes

The authors declare no competing financial interest.

■ ACKNOWLEDGMENTS

This work was supported by the National Science Foundation (award no. DMR-1809092) and Clemson University. We thank Dr. Michael Walter and Daniel Cohen of UNC, Charlotte for their assistance with EQE measurements.

■ REFERENCES

(1) Grätzel, M. Recent Advances in Sensitized Mesoscopic Solar Cells. *Acc. Chem. Res.* **2009**, *42*, 1788−1798.

(2) Hagfeldt, A.; Boschloo, G.; Sun, L.; Kloo, L.; Pettersson, H. Dye-Sensitized Solar Cells. *Chem. Rev.* **2010**, *110*, 6595−6663.

(3) Hedley, G. J.; Ruseckas, A.; Samuel, I. D. W. Light Harvesting for Organic Photovoltaics. *Chem. Rev.* **2017**, *117*, 796−837.

(4) Panda, D. K.; Goodson, F. S.; Ray, S.; Lowell, R.; Saha, S. Multichromophoric Dye-Sensitized Solar Cells Based on Supramolecular Zinc-Porphyrin···Perylene-Imide Dyads. *Chem. Commun.* **2012**, *48*, 8775−8777.

(5) Panda, D. K.; Goodson, F. S.; Ray, S.; Saha, S. Dye-Sensitized Solar Cells Based on Multichromophoric Supramolecular Light-Harvesting Materials. *Chem. Commun.* **2014**, *50*, 5358−5360.

(6) Kitagawa, S.; Kitaura, R.; Noro, S. Functional Porous Coordination Polymers. *Angew. Chem., Int. Ed.* **2004**, *43*, 2334−2375.

(7) Furukawa, H.; Cordova, K. E.; O'Keeffe, M.; Yaghi, O. M. The Chemistry and Applications of Metal-Organic Frameworks. *Science* **2013**, *341*, No. 1230444.

(8) Li, B.; Chrzanowski, M.; Zhang, Y.; Ma, S. Applications of Metal-Organic Frameworks Featuring Multi-Functional Sites. *Coord. Chem. Rev.* **2016**, *307*, 106−129.

(9) Sun, L.; Campbell, M. G.; Dincă, M. Electrically Conductive Porous Metal−Organic Frameworks. *Angew. Chem., Int. Ed.* **2016**, *55*, 3566−3579.

(10) Sheberla, D.; Sun, L.; Blood-Forsythe, M. A.; Er, S.; Wade, C. R.; Brozek, C. K.; Aspuru-Guzik, A.; Dincă, M. High Electrical Conductivity in Ni_3(2,3,6,7,10,11-hexaiminotriphenylene)$_2$, a Semiconducting Metal−Organic Graphene Analogue. *J. Am. Chem. Soc.* **2014**, *136*, 8859−8862.

(11) Dou, J.; Sun, L.; Ge, Y.; Li, W.; Hendon, C. H.; Li, J.; Gul, S.; Yano, J.; Stach, E. A.; Dincă, M. Signature of Metallic Behavior in the Metal−Organic Frameworks M_3(hexaiminobenzene)$_2$ (M = Ni, Cu). *J. Am. Chem. Soc.* **2017**, *139*, 13608−13611.

(12) Park, S. S.; Hontz, E. R.; Sun, L.; Hendon, C. H.; Walsh, A.; Van Voorhis, T.; Dincă, M. Cation-Dependent Intrinsic Electrical Conductivity in Isostructural Tetrathiafulvalene-Based Microporous Metal−Organic Frameworks. *J. Am. Chem. Soc.* **2015**, *137*, 1774−1777.

(13) Talin, A. A.; Centrone, A.; Ford, A. C.; Foster, M. E.; Stavila, V.; Haney, P.; Kinney, R. A.; Szalai, V.; Gabaly, F. E.; Yoon, H. P.; Léonard, F.; Allendorf, M. D. Tunable Electrical Conductivity in Metal-Organic Framework Thin-Film Devices. *Science* **2014**, *343*, 66−69.

(14) Guo, Z.; Panda, D. K.; Maity, K.; Lindsey, D.; Parker, T. G.; Albrecht-Schmitt, T. E.; Barreda-Esparza, J. L.; Xiong, P.; Zhou, W.; Saha, S. Modulating Electrical Conductivity of Metal−Organic Framework Films with Intercalated Guest π-Systems. *J. Mater. Chem. C* **2016**, *4*, 894−899.

(15) Guo, Z.; Panda, D. K.; Gordillo, M. A.; Khatun, A.; Wu, H.; Zhou, W.; Saha, S. Lowering Band Gap of an Electroactive Metal−Organic Framework via Complementary Guest Intercalation. *ACS Appl. Mater. Interfaces* **2017**, *9*, 32413−32417.

(16) Goswami, S.; Ray, D.; Otake, K.-I.; Kung, C.-W.; Garibay, S. J.; Islamoglu, T.; Atilgan, A.; Cui, Y.; Cramer, C. J.; Farha, O. K.; Hupp, J. T. A Porous, Electrically Conductive Hexa-Zirconium(iv) Metal−Organic Framework. *Chem. Sci.* **2018**, *9*, 4477−4482.

(17) Stavila, V.; Talin, A. A.; Allendorf, M. D. MOF-Based Electronic and Optoelectronic Devices. *Chem. Soc. Rev.* **2014**, *43*, 5994−6010.

(18) Zhang, T.; Lin, W. Metal−Organic Frameworks for Artificial Photosynthesis and Photocatalysis. *Chem. Soc. Rev.* **2014**, *43*, 5982−5993.

(19) So, M. C.; Weiderrecht, G. P.; Mondloch, J. E.; Hupp, J. T.; Farha, O. K. Metal−Organic Framework Materials for Light-Harvesting and Energy Transfer. *Chem. Commun.* **2015**, *51*, 3501−3510.

(20) Kaur, R.; Kim, K.-H.; Paul, A. K.; Deep, A. Recent Advances in the Photovoltaic Applications of Coordination Polymers and Metal Organic Frameworks. *J. Mater. Chem. A* **2016**, *4*, 3991−4002.

(21) Dolgopolova, E. A.; Shustova, N. B. Metal-Organic Framework Photophysics: Optoelectronic Devices, Photoswitches, Sensors, and Photocatalysts. *MRS Bull.* **2016**, *41*, 890−896.

(22) Stassen, I.; Burtch, N.; Talin, A.; Falcaro, P.; Allendorf, M.; Ameloot, R. An Updated Roadmap for the Integration of Metal−Organic Frameworks with Electronic Devices and Chemical Sensors. *Chem. Soc. Rev.* **2017**, *46*, 3185−3241.

(23) Paz, F. A. A.; Klinowski, J.; Viela, S. M. F.; Tomé, J. P. C.; Cavaleiro, J. A. S.; Rocha, J. Ligand Design for Functional Metal−Organic Frameworks. *Chem. Soc. Rev.* **2012**, *41*, 1088−1110.

(24) Lu, W.; Wei, Z.; Gu, Z.-Y.; Liu, T.-F.; Park, J.; Park, J.; Tian, J.; Zhang, M.; Zhang, Q.; Gentle, T., III; Bosch, M.; Zhou, H.-C. Tuning Structure and Function of Metal−Organic Frameworks via Linker Design. *Chem. Soc. Rev.* **2014**, *43*, 5561−5593.

(25) Foster, M. E.; Azoulay, J. D.; Wong, B. M.; Allendorf, M. E. Novel Metal−Organic Framework Linkers for Light Harvesting Applications. *Chem. Sci.* **2014**, *5*, 2081−2090.

(26) D'Alessandro, D. M. Exploiting Redox Activity in Metal−Organic Frameworks: Concepts, Trends and Perspectives. *Chem. Commun.* **2016**, *52*, 8957−8971.

(27) Allendorf, M. D.; Foster, M. E.; Léonard, F.; Stavila, V.; Feng, P. L.; Doty, F. P.; Leong, K.; Ma, E. Y.; Johnston, S. R.; Talin, A. A. Guest-Induced Emergent Properties in Metal−Organic Frameworks. *J. Phys. Chem. Lett.* **2015**, *6*, 1182−1195.

(28) Ullman, A. M.; Brown, J. W.; Foster, M. E.; Léonard, F.; Leong, K.; Stavila, V.; Allendorf, M. D. Transforming MOFs for Energy Applications Using Guest@MOF Concept. *Inorg. Chem.* **2016**, *55*, 7233−7249.

(29) Liu, J.; Wöll, C. Surface-Supported Metal−Organic Framework Thin Films: Fabrication Methods, Applications, and Challenges. *Chem. Soc. Rev.* **2017**, *46*, 5730−5770.

(30) Van Gough, D.; Lambert, T. N.; Wheeler, D. R.; Rodriguez, M. A.; Brumbach, M. T.; Allendorf, M. D.; Spoerke, E. D. Controlled

DOI: 10.1021/acsami.8b17807
ACS Appl. Mater. Interfaces 2019, 11, 3196−3206

Nucleation and Growth of Pillared Paddlewheel Framework Nanostacks onto Chemically Modified Surfaces. *ACS Appl. Mater. Interfaces* **2014**, *6*, 1509−1514.
(31) Zacher, D.; Baunemann, A.; Hermes, S.; Fischer, R. A. Deposition of Microcrystalline $[Cu_3(btc)_2]$ and $[Zn_2(bdc)_2(dabco)]$ at Alumina and Silica Surfaces Modified with Patterned Self-Assembled Organic Monolayers: Evidence of Surface Selective and Oriented Growth. *J. Mater. Chem.* **2007**, *17*, 2785−2792.
(32) Shekhah, O.; Wang, H.; Paradinas, M.; Ocal, C.; Schüpbach, B.; Terfort, A.; Zacher, D.; Fischer, R. A.; Wöll, C. Controlling Interpenetration in Metal−Organic Frameworks by Liquid-Phase Epitaxy. *Nat. Mater.* **2009**, *8*, 481−484.
(33) Zacher, D.; Yusenko, K.; Betard, A.; Henke, S.; Molon, M.; Ladnorg, T.; Shekhah, O.; Schupbach, B.; Arcos, T. D. L.; Krasnopolski, M.; Meilikhov, M.; Winter, J.; Terfort, A.; Wöll, C.; Fischer, R. A. Liquid-Phase Epitaxy of Multicomponent Layer-Based Porous Coordination Polymer Thin Films of [M(L)(P)0.5] Type: Importance of Deposition Sequence on the Oriented Growth. *Chem. Eur. J.* **2011**, *17*, 1448−1455.
(34) So, M. C.; Jin, S.; Son, H.-J.; Wiederrecht, G. P.; Farha, O. K.; Hupp, J. T. Layer-by-Layer Fabrication of Oriented Porous Thin Films Based on Porphyrin-Containing Metal−Organic Frameworks. *J. Am. Chem. Soc.* **2013**, *135*, 15698−15701.
(35) Chernikova, V.; Shekhah, O.; Eddaoudi, M. Advanced Fabrication Method for the Preparation of MOF Thin Films: Liquid-Phase Epitaxy Approach Meets Spin Coating Method. *ACS Appl. Mater. Interfaces* **2016**, *8*, 20459−20464.
(36) Zhuang, J.-L.; Terfort, A.; Wöll, C. Formation of Oriented and Patterned Films of Metal−Organic Frameworks by Liquid Phase Epitaxy: A Review. *Coord. Chem. Rev.* **2016**, *307*, 391−424.
(37) Li, J.-R.; Sculley, J.; Zhou, H.-C. Metal−Organic Frameworks for Separations. *Chem. Rev.* **2012**, *112*, 869−932.
(38) Liu, J.; Chen, L.; Cui, H.; Zhang, J.; Zhang, L.; Su, C.-Y. Application of Metal−Organic Frameworks in Heterogeneous Supramolecular Catalysis. *Chem. Soc. Rev.* **2014**, *43*, 6011−6061.
(39) Li, Y.; Pang, A.; Wang, C.; Wei, M. Metal−Organic Frameworks: Promising Materials for Improving the Open Circuit Voltage of Dye-Sensitized Solar Cells. *J. Mater. Chem.* **2011**, *21*, 17259−17264.
(40) Li, Y.; Chen, C.; Sun, X.; Dou, J.; Wei, M. Metal−Organic Frameworks at Interfaces in Dye-Sensitized Solar Cells. *ChemSusChem* **2014**, *7*, 2469−2472.
(41) Fan, S.-Q.; Kim, C.; Fang, B.; Liao, K.-X.; Yang, G.-J.; Li, C.-J.; Kim, J.-J.; Ko, J. Improved Efficiency of over 10% in Dye-Sensitized Solar Cells with a Ruthenium Complex and an Organic Dye Heterogeneously Positioning on a Single TiO_2 Electrode. *J. Phys. Chem. C* **2011**, *115*, 7747−7754.
(42) Lopez, H. A.; Dhakshinamoorthy, A.; Ferrer, B.; Atienzar, P.; Alvaro, M.; Garcia, H. Photochemical Response of Commercial MOFs: $Al_2(BDC)_3$ and Its Use as Active Material in Photovoltaic Devices. *J. Phys. Chem. C* **2011**, *115*, 22200−22206.
(43) Feldblyum, J. I.; Keenan, E. A.; Matzger, A. J.; Maldonado, S. Photoresponse Characteristics of Archetypal Metal-Organic Frameworks. *J. Phys. Chem. C* **2012**, *116*, 3112−3121.
(44) Lee, D. Y.; Shinde, D. V.; Yoon, S. J.; Cho, K. N.; Lee, W.; Shrestha, N. K.; Han, S.-H. Cu-Based Metal−Organic Frameworks for Photovoltaic Application. *J. Phys. Chem. C* **2014**, *118*, 16328−16334.
(45) Lee, D. Y.; Shin, C. Y.; Yoon, S. J.; Lee, H. Y.; Lee, W.; Shrestha, N. K.; Lee, J. K.; Han, S.-H. Enhanced Photovoltaic Performance of Cu-based Metal-Organic Frameworks Sensitized Solar Cell by Addition of Carbon Nanotubes. *Sci. Rep.* **2014**, *4*, No. 3930.
(46) Lee, D. Y.; Kim, E.-K.; Shin, C. Y.; Shinde, D. V.; Lee, W.; Shrestha, N. K.; Lee, J. K.; Han, S.-H. Layer-by-Layer Deposition and Photovoltaic Property of Ru-based Metal−Organic Frameworks. *RSC Adv.* **2014**, *4*, 12037−12042.
(47) Lee, D. Y.; Lim, S.; Shin, C. Y.; Patil, S. A.; Lee, W.; Shrestha, N. K.; Lee, J. K.; Han, S.-H. Facile Interfacial Charge Transfer Across Hole Doped Cobalt-based MOFs/TiO_2 Nano-hybrids Making MOFs Light Harvesting Active Layers in Solar Cells. *J. Mater. Chem. A* **2015**, *3*, 22669−22676.
(48) Chung, H.; Barron, P. M.; Novotny, R. W.; Son, H.-T.; Hu, C.; Choe, W. Structural Variation in Porphyrin Pillared Homologous Series: Influence of Distinct Coordination Centers for Pillars on Framework Topology. *Cryst. Growth Des.* **2009**, *9*, 3327−3332.
(49) Choi, E.-Y.; Barron, P. M.; Novotny, R. W.; Son, H.-T.; Hu, C.; Choe, W. Pillared Porphyrin Homologous Series: Intergrowth in Metal-Organic Frameworks. *Inorg. Chem.* **2009**, *48*, 426−428.
(50) Barron, P. M.; Wray, C. A.; Hu, C.; Guo, Z.; Choe, W. A Bioinspired Synthetic Approach for Building Metal−Organic Frameworks with Accessible Metal Centers. *Inorg. Chem.* **2010**, *49*, 10217−10219.
(51) Gao, W.-Y.; Chrzanowski, M.; Ma, S. Metal-Metalloporphyrin Frameworks: Resurging Class of Functional Materials. *Chem. Soc. Rev.* **2014**, *43*, 5841−5866.
(52) Park, H. J.; So, M. C.; Gosztola, D.; Wiederrecht, G. P.; Emery, J. D.; Martinson, A. B. F.; Er, S.; Wilmer, C. E.; Vermeule, N. A.; Aspuru-Guzik, A.; Stoddart, J. F.; Farha, O. K.; Hupp, J. T. Layer-by-Layer Assembled Films of Perylene Diimide- and Squarene-Containing Metal−Organic Framework-Like Materials: Solar Energy Capture and Directional Energy Transfer. *ACS Appl. Mater. Interfaces* **2016**, *8*, 24983−24988.
(53) Maza, W. A.; Ahrenholtz, S. R.; Epley, C. C.; Day, C. S.; Morris, A. J. Photophysical Characterization of a Ruthenium(II) Tris (2,2-Bipyridine)-Doped Zirconium UiO-67 Metal Organic Framework Thin Film. *J. Phys. Chem. C* **2014**, *118*, 14200−14210.
(54) Williams, D. E.; Shustova, N. B. Metal−Organic Frameworks as a Versatile Tool to Study and Model Energy Transfer. *Chem. Eur. J.* **2015**, *21*, 15474−15479.
(55) Lee, C. Y.; Farha, O. K.; Hong, B. J.; Sarjeant, A. A.; Nguyen, S. T.; Hupp, J. T. Light-Harvesting Metal−Organic Frameworks (MOFs): Efficient Strut-to-Strut Energy Transfer in Bodipy and Porphyrin-Based MOFs. *J. Am. Chem. Soc.* **2011**, *133*, 15858−15861.
(56) Fateeva, A.; Chater, P. A.; Ireland, C. P.; Tahir, A. A.; Khimyak, Y. Z.; Wiper, P. V.; Darwent, J. R.; Rosseinsky, M. J. A Water-Stable Porphyrin-Based Metal−Organic Framework Active for Visible-Light Photocatalysis. *Angew. Chem., Int. Ed.* **2012**, *51*, 7440−7444.
(57) Son, H.-J.; Jin, S.; Patwardhan, S.; Wezenberg, S. J.; Jeong, N. C.; So, M.; Wilmer, C. E.; Sarjeant, A. A.; Schatz, G. C.; Snurr, R. Q.; Farha, O. K.; Wiederrecht, G. P.; Hupp, J. T. Light-Harvesting and Ultrafast Energy Migration in Porphyrin-Based Metal−Organic Frameworks. *J. Am. Chem. Soc.* **2013**, *135*, 862−869.
(58) Liu, J.; Zhou, W.; Liu, J.; Howard, I.; Kilibarda, G.; Schlabach, S.; Coupry, D.; Addicoat, M.; Yoneda, S.; Tsutsui, Y.; Sakurai, T.; Seki, S.; Wang, Z.; Lindemann, P.; Redel, E.; Heine, T.; Wöll, C. Photoinduced Charge-Carrier Generation in Epitaxial MOF Thin Films: High Efficiency as a Result of an Indirect Electronic Band Gap? *Angew. Chem., Int. Ed.* **2015**, *54*, 7441−7445.
(59) Liu, J.; Zhou, W.; Liu, J.; Fujimori, Y.; Higashino, T.; Imahori, H.; Jiang, X.; Zhao, J.; Sakurai, T.; Hattaori, Y.; Matsuda, W.; Seki, S.; Garlapati, S. K.; Dasgupta, S.; Redel, E.; Sun, L.; Wöll, C. A New Class of Epitaxial Porphyrin Metal−Organic Framework Thin-Films with Extremely High Photocarrier Generation Efficiency: Promising Materials for All Solid-State Solar Cells. *J. Mater. Chem. A* **2016**, *4*, 12739−12747.
(60) Spoerke, E. D.; Small, L. J.; Foster, M. E.; Wheeler, J.; Ullman, A. M.; Stavila, V.; Rodriguez, M.; Allendorf, M. D. MOF-Sensitized Solar Cells Enabled by a Pillared Porphyrin. *J. Phys. Chem. C* **2017**, *121*, 4816−4824.
(61) Joyce, J. T.; Laffir, F. R.; Silien, C. Layer-by-Layer Growth and Photocurrent Generation in Metal−Organic Framework Films. *J. Phys. Chem. C* **2013**, *117*, 12502−12509.
(62) Maza, W. A.; Haring, A. J.; Ahrenholtz, S. R.; Epley, C. C.; Lin, S. Y.; Morris, A. J. Ruthenium(II)-Polypyridyl Zirconium(IV) Metal−Organic Frameworks As a New Class of Sensitized Solar Cells. *Chem. Sci.* **2016**, *7*, 719−727.
(63) Goswami, S.; Ma, L.; Martinson, A. B. F.; Wasielewski, M. R.; Farha, O. K.; Hupp, J. T. Toward Metal−Organic Framework-Based

DOI: 10.1021/acsami.8b17807
ACS Appl. Mater. Interfaces 2019, 11, 3196−3206

Solar Cells: Enhancing Directional Exciton Transport by Collapsing Three-Dimensional Film Structures. *ACS Appl. Mater. Interfaces* **2016**, *8*, 30863−30870.
(64) Chueh, C.-C.; Li, C.-Z.; Jen, A. K.-Y. Recent Progress and Perspective in Solution-Processed Interfacial Materials for Efficient and Stable Polymer and Organometal Pervoskite Solar Cells. *Energy Environ. Sci.* **2015**, *8*, 1160−1189.
(65) Rudolph, M.; Yoshida, T.; Miura, H.; Schlettwein, D. Improvement of Light-Harvesting by Addition of a Long-Wavelength Absorber in Dye-Sensitized Solar Cells Based on ZnO and Indoline Dyes. *J. Phys. Chem. C* **2015**, *119*, 1298−1311.
(66) Guldi, D. M.; Hirsch, A.; Scheloske, M.; Dietel, E.; Troisi, A.; Zerbetto, F.; Prato, M. Modulating Charge-Transfer Interactions in Topologically Different Porphyrin−C_{60} Dyads. *Chem. Eur. J.* **2003**, *9*, 4968−4979.
(67) Ahn, D. Y.; Lee, D. K.; Shin, C. Y.; Bui, H. T.; Shrestha, N. K.; Giebeler, L.; Noh, Y.-Y.; Han, S.-H. Novel Solid-State Solar Cell Based on Hole-Conducting MOF-Sensitizer Demonstrating Power Conversion Efficiency of 2.1%. *ACS Appl. Mater. Interfaces* **2017**, *9*, 12930−12935.
(68) Wang, Q.; Moser, J.-E.; Grätzel, M. Electrochemical Impedance Spectroscopic Analysis of Dye-Sensitized Solar Cells. *J. Phys. Chem. B* **2005**, *109*, 14945−14953.
(69) Wu, W.-Q.; Xu, Y.-F.; Su, C.-Y.; Kuang, D.-B. Ultra-long Anatase TiO_2 Nanowire Arrays with Multi-Layered Configuration on FTO Glass for High-Frequency Dye-Sensitized Solar Cells. *Energy Environ. Sci.* **2014**, *7*, 644−649.
(70) Sarker, S.; Ahammad, A. J. S.; Seo, H. W.; Kim, D. M. Electrochemical Impedance Spectra of Dye-Sensitized Solar Cells: Fundamental Spreadsheet Calculation. *Int. J. Photoenergy* **2014**, No. 851705.

DOI: 10.1021/acsami.8b17807
ACS Appl. Mater. Interfaces 2019, 11, 3196−3206